International Journal of Fluid Machinery and Systems DOI: 10.5293/IJFMS.20xx.x.x.xxx
Vol. x, No. x, October-December 20xx (This information will be given when accepted) ISSN (Online): 1882-9554

Original Paper

Estimating the energy loss in Pelton turbine casings by transient CFD and experimental analysis

S Petley, G A Aggidis

Lancaster University Renewable Energy Group and Fluid Machinery Group, Engineering Department, Lancaster University, Lancaster, LA1 4YR, UK
s.petley@lancaster.ac.uk, g.aggidis@lancaster.ac.uk

Abstract

Many consider the Pelton turbine a mature technology, nevertheless the advent of Computational Fluid Dynamics (CFD) in recent decades has been a key driver in the continued design development. Impulse turbine casings play a very important role and experience dictates that the efficiency of a Pelton turbine is closely dependent on the success of keeping vagrant spray water away from the turbine runner and the water jet. Despite this overarching purpose, there is no standard design guidelines and casing styles vary from manufacturer to manufacturer, often incorporating a considerable number of shrouds and baffles to direct the flow of water into the tailrace with minimal interference with the aforementioned. The present work incorporates the Reynolds-averaged Navier Stokes (RANS) k-ε turbulence model and a two-phase Volume of Fluid (VOF) model, using the ANSYS® FLUENT® code to simulate the casing flow in a 2-jet horizontal axis Pelton turbine. The results of the simulation of two casing configurations are compared against flow visualisations and measurements obtained from a model established at the National Technical University of Athens. Further investigations were carried out in order to compare the absolute difference between the numerical runner efficiency and the experimental efficiency. In doing so, the various losses that occur during operation of the turbine can be appraised and a prediction of casing losses can be made. Firstly, the mechanical losses of the test rig are estimated to determine the experimental hydraulic efficiency. Following this, the numerical efficiency of the runner can then be ascertained by considering the upstream pipework losses and the aforementioned runner simulations, which are combined with previously published results of the 3D velocity profiles obtained from simulating the injectors. The results indicate that out of all of the experimental cases tested, in the best case scenario the casing losses can be approximated to be negligible and in the worst case scenario ≈3%.

1. Introduction

The casing of a Pelton turbine is an important component as it collects the water leaving the runner. Some of this water generates splashing and spray, which may cause interference with the runner and water jet, thereby reducing the efficiency. Therefore the design of the casing as a means to reduce this impact is of interest to manufactures [1].

In recent decades, numerical tools such as Computational Fluid Dynamics (CFD) have been applied to the development of Pelton turbines, more specifically the individual components are treated in isolation and the resulting high fidelity models offer a good prediction of the reasonable gains in efficiency from the optimisation of each component. To date, CFD has been used to analyse and further develop the injector and runner design leading to noticeable improvements, however analysis of the flow within the casing remains complex and as such there are no available studies in the public domain, documenting how Eulerian mesh based CFD solvers can be used for this task, highlighting the knowledge gap and novelty of this research.

As an alternative approach, some researchers have developed Lagrangian particle based methods. Neuhauser et al. [2] and Rentschler et al. [3], both of Andritz Hydro, documented how the in-house SPH-ALE solver can be used to model the free surface flow in the casing of a Pelton turbine, with the aim of evaluating the potential for improvement of efficiency by additional casing components in rehabilitation projects. However, they note it has taken 12 years to develop the code. Moreover, thanks to the recent improvement in computer hardware, larger two-phase unsteady models can be studied in shorter timescales.

On the basis of the above considerations, this paper will demonstrate how the Reynolds-averaged Navier Stokes (RANS) k-ε turbulence model and a two-phase Volume of Fluid (VOF) model within the ANSYS® FLUENT® code can be employed as a visualisation tool to investigate casing flows and improve the design of a 2-jet horizontal axis Pelton turbine. Furthermore, this paper will attempt to quantify the energy loss due to the casing by comparison of the results obtained with the CFD models and experimental testing.

Initial experimental measurements were carried out at the Laboratory for Hydraulic Machines, National Technical University of Athens (NTUA) and are outlined in Section 2.

2. Experimental Results

The experimental results were carried out using the Pelton test rig at NTUA, shown in Fig. 1. A high head adjustable speed multistage pump of nominal operation point Q=290 m^3/hr, H=130 mWG, coupled via a hydraulic coupler to a 200 kW induction motor is used to feed the model turbine, pumping from the 320 m^3 main reservoir of the lab. The tests were carried out using the twin jet Z120 Pelton manufactured by Gilbert Gilkes & Gordon Ltd, which was coupled to a 75kW DC generator with continuous speed regulation.

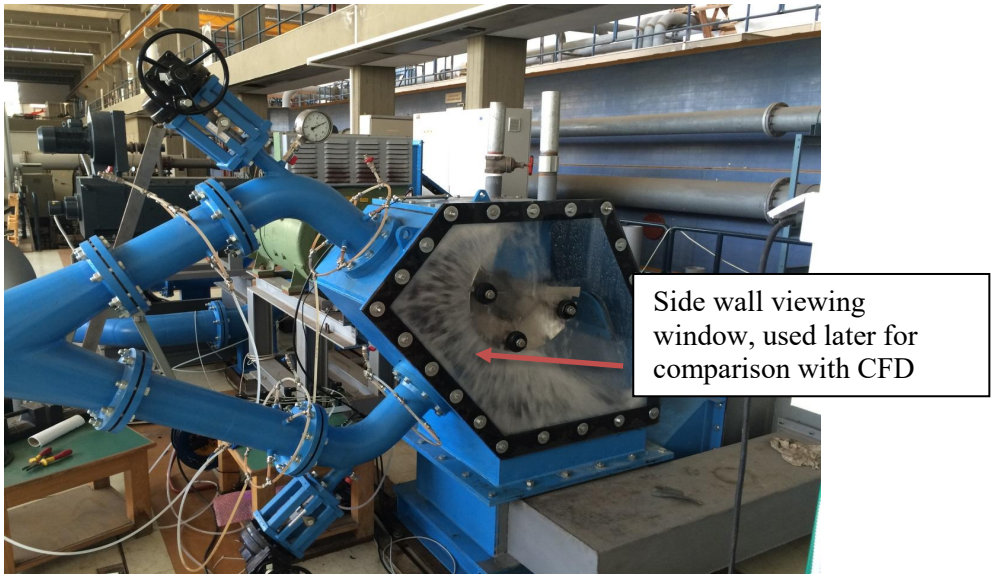

Figure 1. Pelton testing facility at NTUA.

2.1. Uncertainty Analysis

Based on the most recent calibrations the systematic uncertainty for each instrument used during this testing is given in Table 1. Testing and calibration of all the sensors was carried out according to testing standard IEC 60193 [4].

Table 1 Systematic error of each instrument

Instrument	Detail	Systematic Uncertainty
Pressure Transducer (*H*)	ESI Technology, model: Ellison-Pr3200	±0.3%
Flow meter (*Q*)	ABB, model: DE41F	±0.5%
Torque meter (*M*)	Datum Electronics, model: M425	±0.1%
Speed Sensor (*n*)	Efectron, model: GA3005-ANKG	±0.05%

When determining the uncertainty the calibration error for each instrument becomes the systematic uncertainty. The total systematic uncertainty for the hydraulic efficiency, δ_S, can be calculated using eq. (1).

$$\delta_S = \sqrt{{\delta_H}^2 + {\delta_Q}^2 + {\delta_M}^2 + {\delta_n}^2} \quad (1)$$

The total systematic uncertainty in the efficiency, η, was calculated as **±0.6%**. During the experimental testing repeat measurements at a single operating points, known as the control points, were recorded. These were then used to determine the random uncertainty according to the procedure defined in Annex L of the IEC 60193. The standard deviation, s_y, is calculated using eq. (2) below.

$$s_\gamma = \sqrt{\frac{1}{n-1}\sum_{i=1}^{n}(\bar{Y} - Y_i)^2} \quad (2)$$

Where $\bar{Y}$ is the arithmetic mean of the efficiency for n individual measurement points. The random uncertainty associated with the mean value at the 95% confidence level, using the Student's T distribution, is given by eq. (3).

$$s_r = \frac{t \, . \, s_\gamma}{\sqrt{n}} \quad (3)$$

Where t is the Student's T factor, which can be approximated using eq. (4).

$$t = 1.96 + \frac{2.36}{n-1} + \frac{3.2}{(n-1)^2} + \frac{5.2}{(n-1)^{3.84}} \quad (4)$$

The total random uncertainty, δ_R at 95% confidence was calculated using this method as **±0.033%.** Therefore, the total uncertainty, δ_t, was calculated as ±**0.6009%** using eq. (5) below.

$$\delta_t = \sqrt{{\delta_S}^2 + {\delta_R}^2} \quad (5)$$

The characteristic equations of turbine unit speed, n_{11}, and unit flow, Q_{11k}, used to define the operation and performance of the turbine, are given in (6) – (10) below.

$$n_{11} = \frac{n \times D}{\sqrt{H}} \quad (6)$$

$$Q_{11k} = \frac{Q/N_j}{B^2 \times \sqrt{H}} \quad (7)$$

$$P_{out} = M\omega \quad (8)$$

$$P_{in} = \rho g H Q \quad (9)$$

$$\eta = \frac{P_{out}}{P_{in}} \quad (10)$$

Where n is the rotational speed of the runner, H is the net head, Q is the flow rate, N_j is the number of jets, M is the torque measured on the turbine shaft, ρ is the density of water and g is the acceleration due to gravity.

3. Numerical Model

3.1. Physical Conditions

It was noted by Perrig [5] that there are four flow regimes within a Pelton turbine system: i) confined steady-state flows in the upstream pipes and the distributor, ii) free jets past the injector, iii) transient free surface flow in the buckets and iv) dispersed 2-phase flow in the casing, which makes simulation of a full turbine a complex and demanding task. The flow in a Pelton casing is therefore by nature transient, multiphase and turbulent.

Once the water has left the runner the flow is guided to the tailrace by the casing walls and inserts. The flow is highly turbulent and mainly driven by inertia, however, since the Weber number is decreasing the water sheets tend to break up and droplet formation occurs. The kinetic energy is dissipated when the water sheets impact on a solid obstacle or when there is an intersection of one water sheet with another one, subsequently the flow is gravity driven.

3.2. Model Definition

As mentioned previously, all simulations were carried out in FLUENT using the k-ε turbulence model and the VOF multiphase model. Because of the complexity of the analysis, a preliminary in-depth study was carried out to evaluate the influence of the main numerical parameters on the stability of the simulation, in line with [6]. Based on previous studies

in the literature [7] several simplifications can be made to the geometry that will have minimal effect on the predicted flow but which significantly reduce the model size:

- The mounting arms at the rear of the buckets were removed since this will not interact with the water
- Only six (out of the full 18 buckets) were modelled because after some initial noise the flow will interaction with each bucket will be repeatable. Almost all available studies in the literature use a reduced number of buckets [8].
- Only one side of the runner and casing are modelled since the flow can be assumed to be symmetrical, shown in Fig. 2.

It has been shown in previous studies that when the runner is operating under steady state conditions the torque acting on each individual bucket can be considered periodic and therefore many researches use a reduced number of buckets to predict the runner performance. However, since this study is concerned with the flow within the casing it is not known whether it is feasible to use a reduced number of buckets to observe the casing flow. In order to assess the differences between using a reduced number of buckets and a full runner, simulations were carried out with 2, 4, 6 and 18 buckets respectively and the normalised efficiency appears in Table 2. The results indicate a negligible difference of 0.05% efficiency difference between the 6-bucket and 18-bucket simulations. Given that a significant portion of the flow is captured with 6-bucket simulation, all future simulations will use this number.

Table 2. Mesh sizing and normalised efficiency for different bucket number simulations

Mesh #	Number of Elements Runner + Casing [million]	Normalised Efficiency [%]
2-bucket	1.05 + 3.90	**99.88**[1]
4-bucket	1.96 + 3.90	**100.05**
6-bucket	2.87 + 3.90	**100**
18-bucket	8.35 + 3.90	**99.95**

The model consists of two domains, the stationary casing and rotating runner, the runner analysis is a transient simulation and the rotation is modelled using a sliding mesh approach, with an interface defined between the casing and runner domains as shown in Fig. 2.

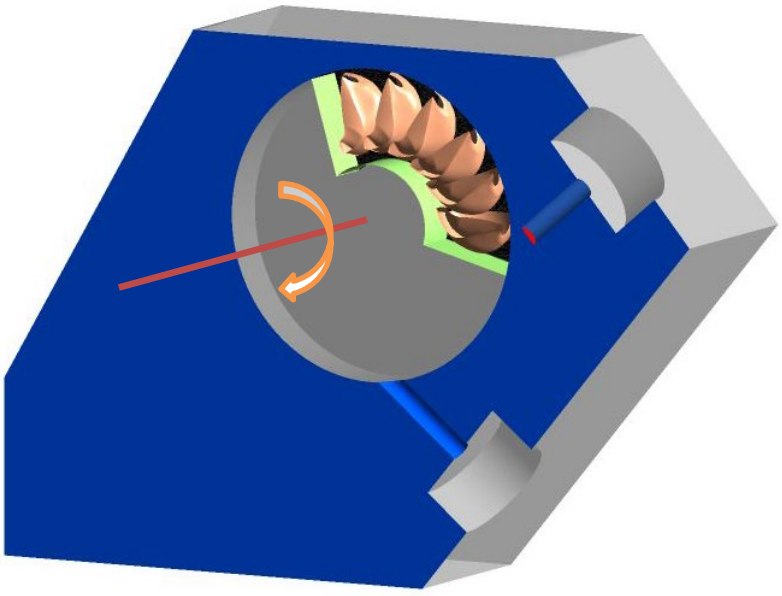

Figure 2. Computational fluid model geometry

The simulations were all carried out at the best efficiency (BEP) speed n_{11} = 39 and the BEP flow rate The meshes consisted of swept hexahedral cells within the stationary jet and a portion of the casing, highlighted in Fig. 4 and fully tetrahedral cells within the runner domain. Face sizing was used to match the element size across the interface in order to minimise numerical diffusion error. Inflation layers were placed on all wall boundaries and the minimum wall distance was calculated to ensure agreement with the acceptable y+ limits for use with wall functions, i.e. 30 < y+ < 300 [9].

[1] Also significant for 2-bucket flow is the final bucket sees the jet switch off, such that there will be a slight reduction in the torque developed on that bucket since the flow into a bucket is significantly affected by how it interacts with the underside of the next bucket. Therefore, as a result the power generated will be lower and hence the efficiency will also be lower. One may conclude that the slightly larger reduction in efficiency can be attributed to this and the real value will in fact be ~99.95%.

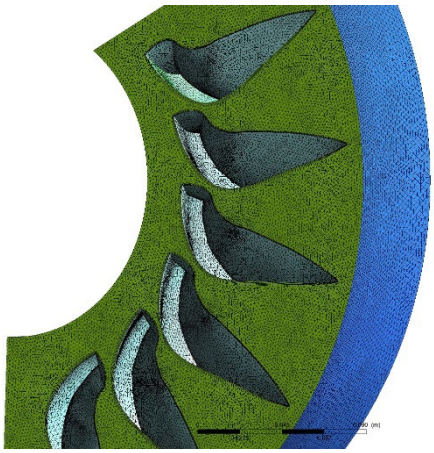

Figure 3. Runner mesh (fully unstructured)

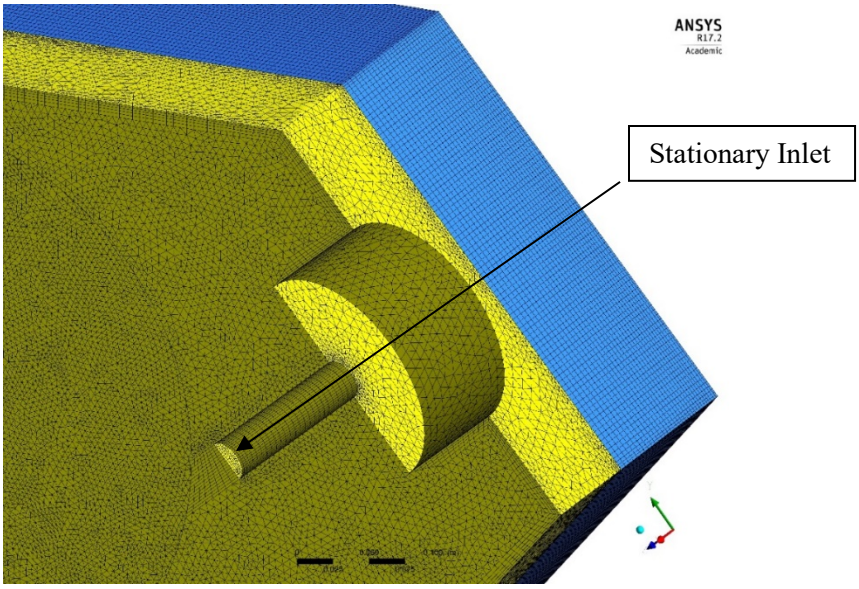

Figure 4. Casing mesh, showing structured (blue) and unstructured (yellow) regions

Although detailed analysis of the flow in the casing consists of plotting the water volume fraction as an isosurface and looking at contour plots of pressure for example, the primary integral quantity that can be measured from these simulations is the runner torque, which allows for the calculation of the runner hydraulic efficiency, as follows. The torque value calculated will be used to compare the effects of mesh and timestep. In FLUENT a moment monitor is defined to measure the torque, which writes out the final value of the moment for each timestep, this is defined for both the inside and outside surfaces (wall zones) of each bucket 1 – 6, highlighted for a representative bucket in Fig. 5.

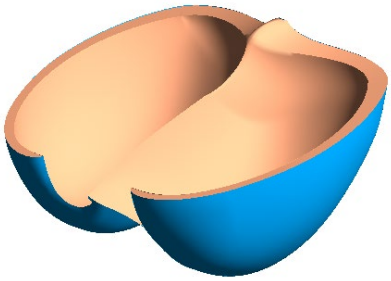

Figure 5. Moment monitor wall zone definition – inside (orange) and outside (blue)

The torque is then numerically integrated using the trapezium rule to give the area under the total torque curve or the work done by a single bucket.

$$W = \int_b^a M(\theta)d\theta = \frac{1}{2}\sum_{i=1}^{n}(M(\theta_{i+1}) + M(\theta_i))(\theta_{i+1} - \theta_i) \qquad (11)$$

The time for a single revolution is calculated is given by eq. (12);

$$t = \frac{2\pi}{\omega} \qquad (12)$$

Using equations (11) and (12), the power produced by the runner, where N_B is the total number of buckets that make up the runner, can be calculated as shown in eq. (13).

$$P_{Out} = \frac{N_B \times W}{t} \tag{13}$$

However, in order to calculate the runner efficiency, the hydraulic power is also required, which can be expressed as eq. (14). Where $\dot{m}$ is the jet mass flow rate [kg s^{-1}] and u is the jet velocity [m s^{-1}], which is defined by the inlet boundary conditions.

$$P_{in} = \frac{\dot{m} \times u^2}{2} \tag{14}$$

Therefore, the efficiency is the ratio of eq. (13) and (14).

Since computational time was a limiting factor for this project it was important to carry out a mesh sensitivity study to determine the effect the mesh size has on the appearance of casing flow, since it is known that an inadequate mesh sizing can smooth free surface interfaces and falsely modify flow features. A Grid Convergence Index (GCI) study, as suggested by Roache [10], was carried out to investigate the discretisation errors introduced by the mesh with respect to the relative mesh refinement. Three meshes were created using a refinement ratio r=1.2 with the coarsest mesh containing 6.77 million elements and the finest mesh containing 11.92 million elements. The results of the three meshes, normalised to the coarsest mesh result are shown in Table 3 below. The results are also plotted in Fig. 6. Furthermore, Table 3 also indicates the time taken for each simulation run using the Lancaster University High End Computing (HEC) cluster on four dedicated 16-core servers (each with two Intel(R) Xeon(R) E5-2640 v3 @ 2.6 GHz processors).

Table 3. Mesh refinement study results normalised to coarse grid

Mesh #	**Normalised Grid Spacing**	**Number of Elements Runner + Casing [million]**	**Normalised Efficiency [%]**	**Wall clock time**
Coarse	1.000	2.87 + 3.90	**100**	31 hr 12 mins
Med	0.833	3.70 + 4.55	**100.688**	56 hr 49 mins
Fine	0.694	5.11 + 6.81	**100.942**	122 hr 08 mins

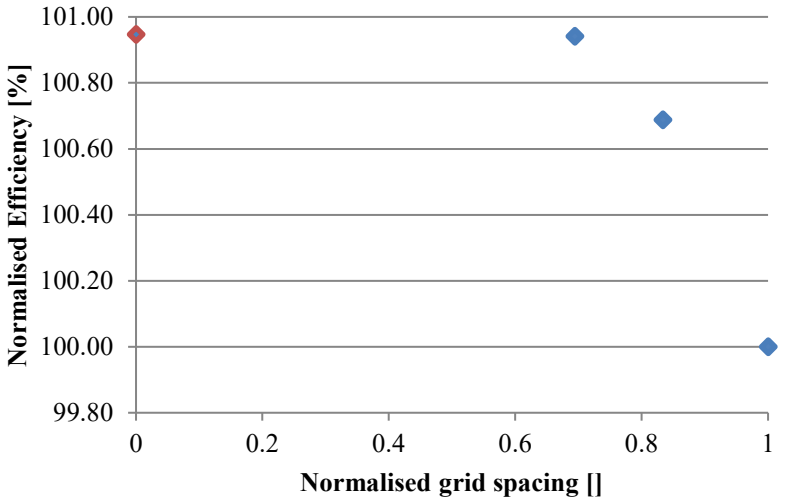

Figure 6. Mesh refinement study results: normalised efficiency against normalised grid spacing

A successive reduction of the grid spacing causes the efficiency to approach the value for the asymptotic zero grid spacing. The order of convergence, pc, can be calculated using eq. (15) is used to calculate with η_n being the efficiency of the respective mesh.

$$p_c = \frac{\ln\left(\frac{\eta_1 - \eta_2}{\eta_2 - \eta_3}\right)}{\ln\ (r)} \tag{15}$$

Furthermore, a Richardson extrapolation of the two finest meshes determines the efficiency of the asymptotic zero grid, $\eta_{h=0}$.

$$\eta_{h=0} = \eta_3 + \frac{\eta_3 - \eta_2}{2^{Pc} - 1} \quad (16)$$

A zero mesh spacing is calculated as 100.95 %. This result is also shown in Fig. 6, which indicates that the coarse mesh will provide mesh independent results.

Furthermore, a timestep study was conducted and a conservative timestep of 3.5219e-5 s, which equates to 0.2 degree rotation was chosen, however Table 4 shows the differences in normalised efficiency for the 4 timestep variations.

The most widely used two equation models in FLUENT are the Realisable k-ε and Menter's k-ω Shear Stress Transport (SST) model [11]. The two models are only subtly different since the SST model is a combination of pure two equation models, namely k-ε is used in the free stream zone, while the k-ω is used near the wall. In order to determine which model to choose two simulations were run using a 2-bucket Pelton runner to assess their influence on performance and computational cost. Based on these results going forward the Realizable k-ε was used as it solved marginally faster.

The most widely used two equation models in FLUENT are the Realisable k-ε and Menter's k-ω Shear Stress Transport (SST) model [90]. The two models are only subtly different since the SST model is a combination of pure two equation models, namely k-ε is used in the free stream zone, while the k-ω is used near the wall. In order to determine which model to choose two simulations were run using a 2-bucket Pelton runner to assess their influence on performance and computational cost. Based on these results going forward the Realizable k-ε was used as it solved marginally faster. A second-order backward Euler scheme is used for the transient terms and a second-order upwind for the spatial discretisation. The convergence criteria for each timestep was chosen to correspond to a rms value of $1x10^{-4}$ for the residuals of the momentum equations. In order to ensure minimal numerical diffusion a compressive scheme for the discretisation of the volume fraction equations was chosen and the surface tension model in FLUENT is the continuum surface force (CSF) model proposed by Brackbill et al [12].

Table 4. Average torque and efficiencies for changing timestep

		Timestep= 0.1 deg	Timestep= 0.2 deg	Timestep= 0.4 deg	Timestep= 0.8 deg
Normalised efficiency	[%]	**100.00%**	**99.503%**	**99.105%**	**98.14%**

The relative numerical errors based on the assumptions are given in Table 5 below[2]. The total numerical error calculated using the root-sum-square method is 0.97%. It should be noted, however, that there could be further sources of error not included, such as surface roughness. There could also be additional errors arising from the RANS modelling approach used.

Table 5. Known relative numerical error band introduced by various assumptions

Source of Error	**Numerical Error Band δ [%]**
Timestep	0.50
Turbulence Modelling	0.47
Periodicity	0.12
Domain Discretisation (Mesh)	0.68
Total (Root-Sum-Square)	**0.97**

3.3. Estimating Efficiency Loss due to Casing

In the previous section 3.2 the method of determining mesh and timestep independence is based upon measuring the torque of the runner developed by the water jet and then using this to work out the efficiency. However, in order to measure the effect on efficiency from the splash water interference the simulation should be run for several runner rotations to establish the flow field within the casing. As a standalone test case, the 18 – bucket runner simulation was run for four full runner revolutions, the torque plots for the first and second bucket have been modelled for the four phases, shown in Fig. 7.

[2] The errors are listed in the relevant sections, for example the timestep error is found as the difference between the normalised efficiency of timestep used in the study (0.2 deg) and the smallest timestep considered (0.1 deg), which equates to 100% – 99.503% = 0.5%

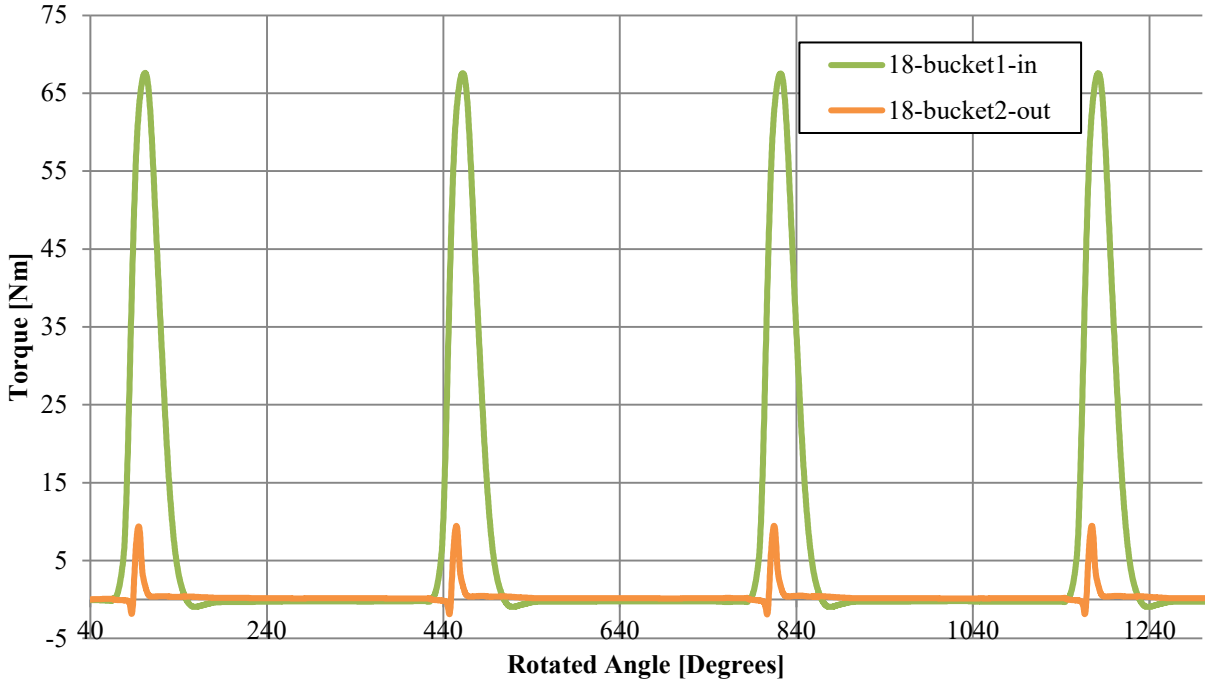

Figure 7. Comparing the torque curves for bucket 1 and 2 during four rotations

As the results indicate the predicted torque experienced on the first two buckets are very similar for the four rotations. This suggests that at the current mesh resolution the splash water is not captured with enough detail to contribute to any significant interference with the runner and therefore influence to generated torque, which would show up after two revolutions when there is a considerable volume of water in the casing. Therefore, it is not possible to make a quantitative prediction of the efficiency of a full Pelton turbine including the casing effects using the simulation described. However, the mesh validation was based on achieving a runner torque value independent of the mesh. Fig. 8 compares the efficiency calculated from the mesh independent runner torque and the highest obtained experimental efficiency reported in this paper for upper jet. The error in the calculation is around 3%, this is slightly lower than the error orders of other numerical analyses carried out on Pelton turbines [6].

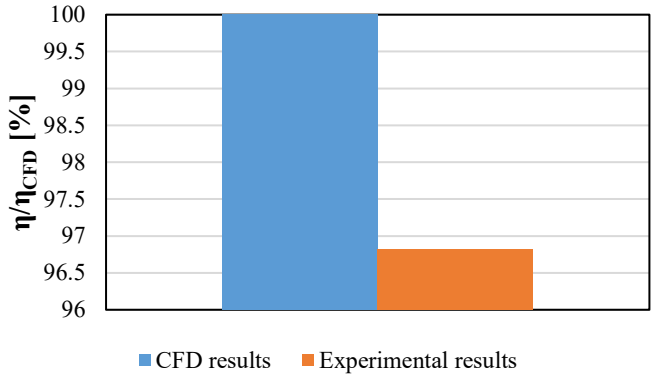

Figure 8. Comparison of the CFD and experimentally obtained efficiency

3.4. Correlating CFD Post Processing with Experiments

The use of advanced image techniques such as LDA and PIV to validate CFD results has been widely documented in the literature [13] [14]. From the PIV data, the mean velocity, turbulent kinetic energy, Reynolds stresses and dissipations rate can all be extracted from the snapshots of instantaneous velocity field. Despite the availability of PIV and similar techniques the CFD results within this study are to be used as a purely visual tool in order to provide detailed information related to the direction of the water flow and not necessarily the velocity, hence the decision to compare the CFD results with visual snapshots obtained from the experimental test rig at NTUA.

Since the initial CFD modelling has been carried out for upper jet only the visual comparison will be made against the experimental test for upper jet operation. Following this the model is then applied for lower jet operation. In Fig. 9 it has been identified that there are three main portions of flow that offer visual comparison to the CFD results.

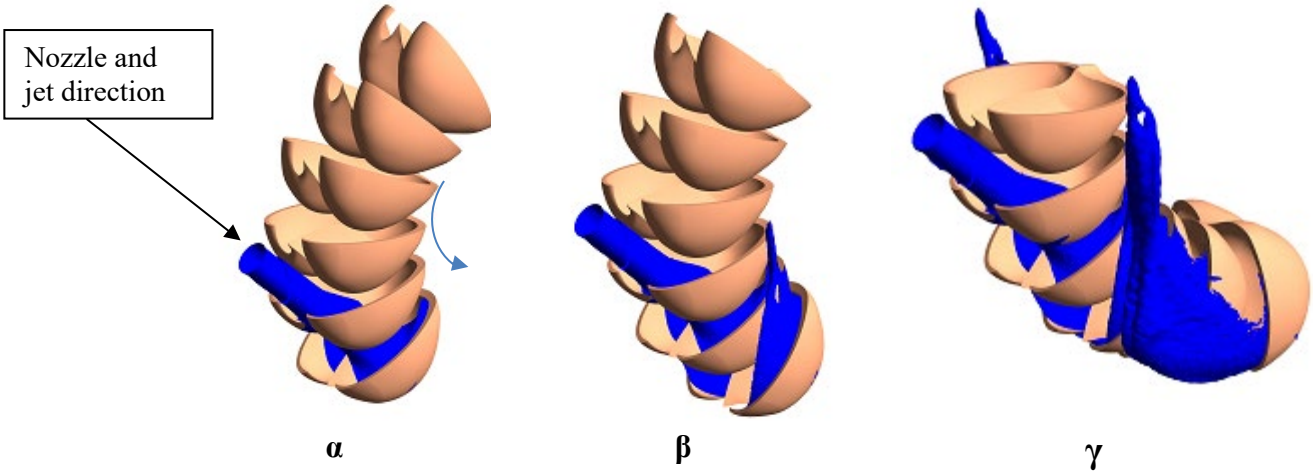

Figure 9. Flow sequence of water leaving the bucket

The first, **α**, is the water that leaves closer to the root and along the sides of the bucket in the first 40° of rotation; this is shown in the first snapshot of the sequence. However not all of the flow can leave the bucket in this first initial stage, this flow can be seen in the right hand side of top right hand quarter of Fig. 10 and leaves more towards the cut-out. This flow still has a remaining portion of axial kinetic energy and makes its way towards the front face of the casing, as identified as the second main portion of flow, **β**. The third main portion, **γ**, identified is the last residual 20% of flow that remains in the bucket after at least 90° of rotation; this is mainly visible as a fine spray mist in the experimental visualisation that travels towards the symmetry plane as a result of high radial but low axial kinetic energy. Once the water has impacted the front face of the casing it dissipates much of its remaining kinetic energy and the major force is now gravitational, it spreads a short distance before falling into the tailrace below, however on the side closest to the injectors this flow tends to recirculate and accumulate in the top left hand side of the casing, where interference with the water jet leaving the injectors occurs.

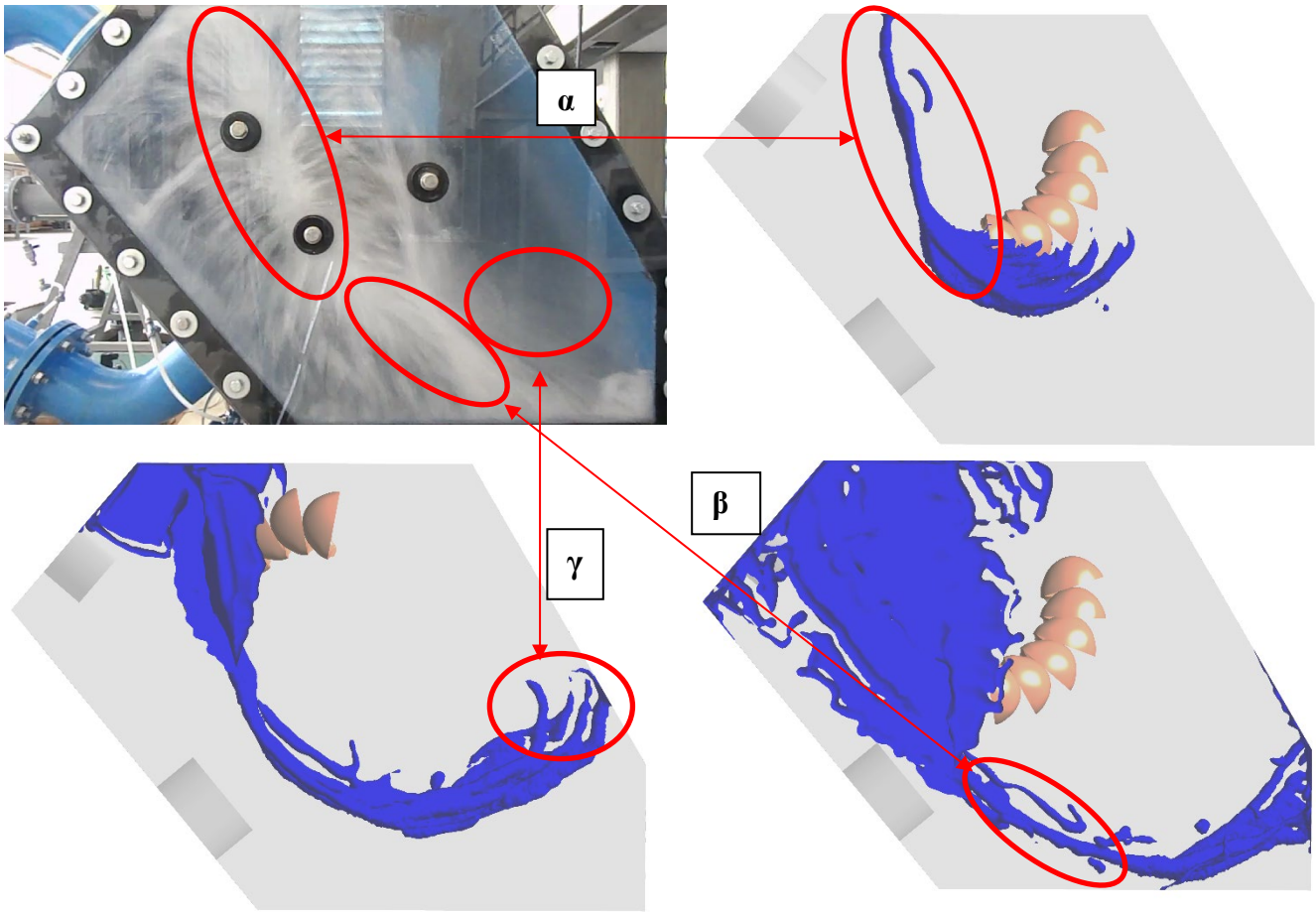

Figure 10. Upper Jet Experimental and 1% water VF plot comparison for 6-bucket coarse mesh at 200º, 360º, 560º rotations at BEP

In the absence of shrouds or baffles the water is allowed to circulate around the casing. It can be noted from the velocity vectors in Fig. 11(δ) that the water in the top left hand corner of the casing is directed towards the symmetry

plane, eventually falling onto the injector and jet. Likewise, in Fig. 11(ε), the water from the lower jet circulates in the top right hand corner before falling onto the runner. It is therefore recommended that a shroud be placed over the injectors and jet to ensure that the quality is not hindered by the splash water interference. Furthermore a curved baffle can be placed around the runner to inhibit water entering the roof of the casing, as recommended in [15].

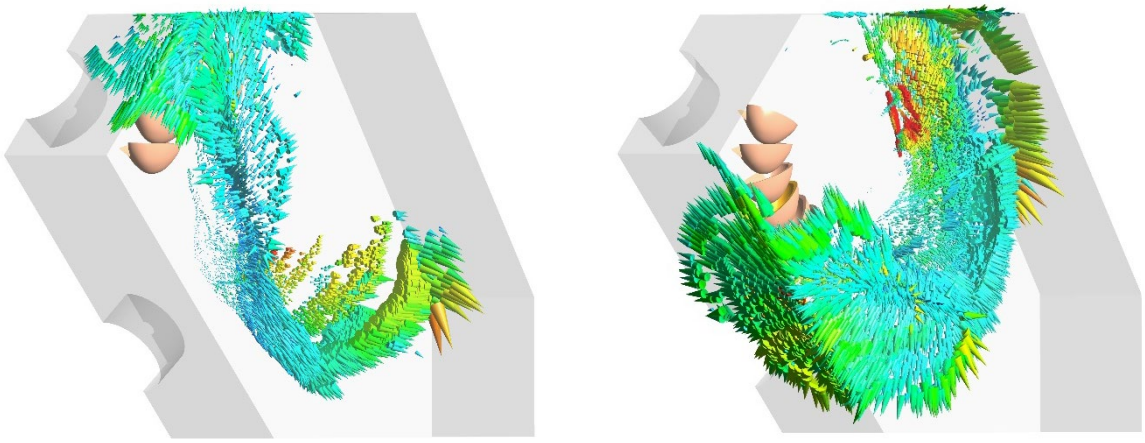

δ ε

Figure 11. Comparison of upper and lower injector

In Fig. 12 efficiency curves for the unit speed, n_{11} = 39, are plotted against a range of non-dimensional flowrate, Q_{11k}, for both the upper jet and lower jet, with and without shrouding, normalised against the lower jet with shrouding, indicating the positive improvement of their installation, particularly at higher flow rates for the lower jet. While it is not yet possible to a make a quantitative prediction of the efficiency of a full Pelton turbine using the simulation described, it has nevertheless been shown by observations of the flow in the casing how baffles and shrouding can be added with positive effect. Since the addition of the curved baffle has very little influence on the flow for the upper jet, the corresponding photograph from experiment is shown for lower jet only in Fig. 13.

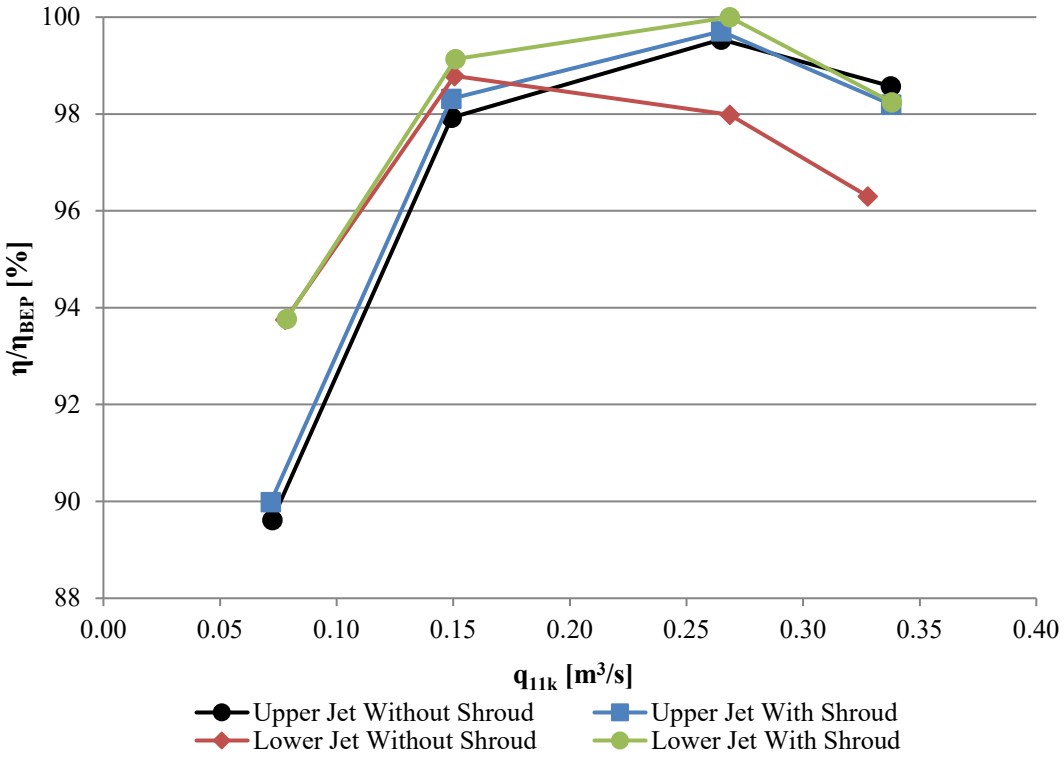

Figure 12. Comparison of experimental results for upper and lower injector with and without baffles and shrouds

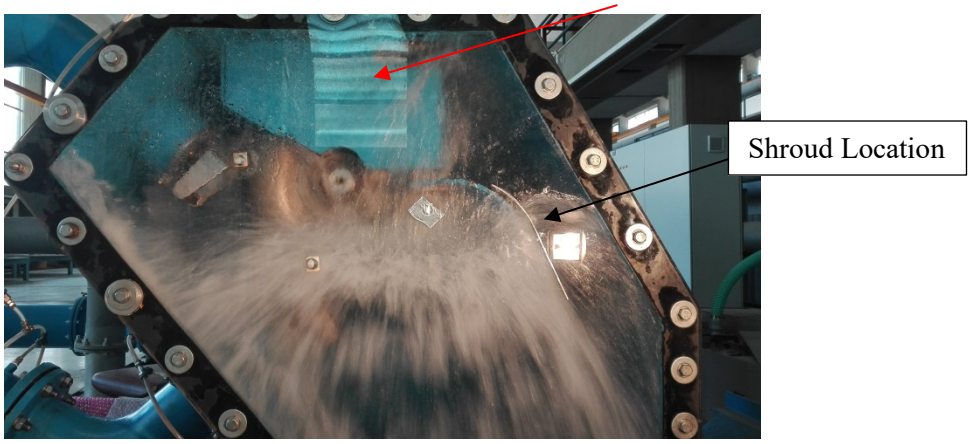

Figure 13. Lower jet with baffles and shrouds

A small portion of flow still enters the roof of the casing, indicated by the red arrow. Therefore, the clearance between the baffle and the runner must be as small as possible to minimise the leakage through the clearance, which is created by the suction in the narrow gap which in turn leads to windage losses.

3.5. Further Investigation of Casing Design Parameters

As previously mentioned very few design guidelines exist in the literature. However some sources [15] [16] [17] list generic dimensions, such as casing width, based on a ratio of bucket width or jet diameter. In this section the CFD model outlined in 3.2. will be used to further investigate the effect of casing width on turbine efficiency. Fig. 14(σ) and Fig. 14(ψ) compare the vector plots for the standard width and 45% of standard respectively for upper jet operation at the same timestep. What is apparent is that the water has considerably higher kinetic energy in the narrower casing at the point it makes contact with the wall and therefore shows noticeably more spreading across the surface. Furthermore, due to the reduced width the water experiences a choking effect when it impacts the top corner, leading to considerable interference and further entrainment with the runner, resulting in higher windage losses, highlighted by the red arrow. In addition to testing the standard casing, and the 45% width a further two widths were considered. In order to carry out these experiments a number of panels separated by spacers into the Pelton test rig at NTUA. The upper jet efficiency curves for the unit speed, n_{11} = 39, are plotted against a range of non-dimensional flowrate, Q_{11k}, as shown in Fig. 15.

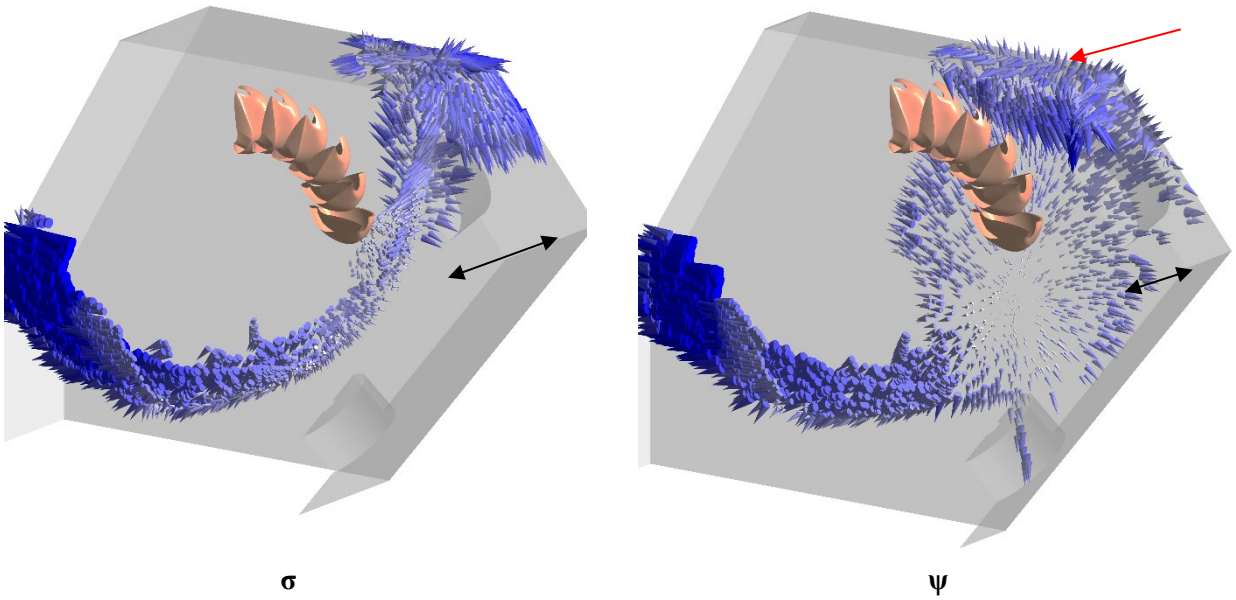

σ ψ

Figure 14. Comparing casing width (black arrows indicating relative width)

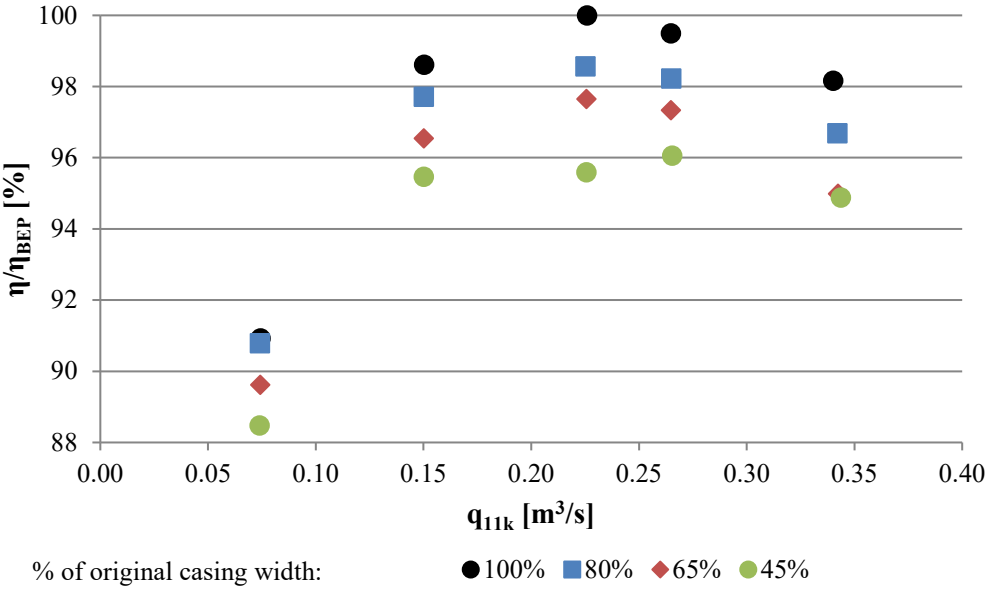

Figure 15. Pelton experimental efficiency curves showing effect of casing width at BEP

Likewise the overall effect of casing width on efficiency at the BEP is indicated in Fig. 16, where there was a reduction of 3.3% in efficiency from the current casing width to the narrowest testing. Since these tests were equipped with the same baffles and shrouds described in 3.3 it is evident that the overall dimensions of the casing have much larger effect on efficiency than the gain made by the addition of the baffle and shrouds.

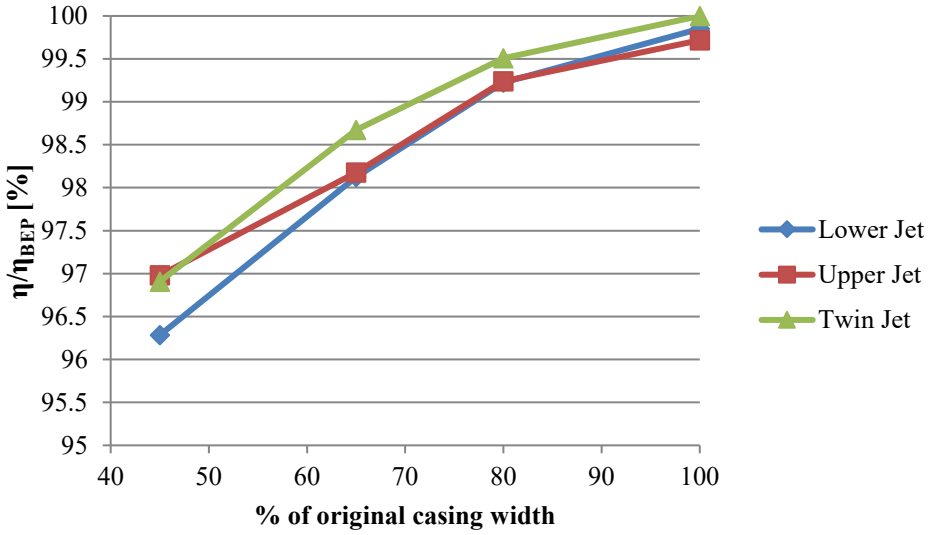

Figure 16. Effect of changing casing width on efficiency at the BEP

4. Loss Analysis of a Typical Experiment and Casing Efficiency

In section 3.3 the error between the numerical and experimental efficiency was estimated as 3%. However, this value does not take into account the various losses in the system, therefore an attempt to quantify the efficiency loss due to the casing has been made by comparing the absolute experimental hydraulic efficiency to the numerical hydraulic efficiency. In order to provide a comparison the measurements of the upper and twin jet results with the original casing width in Fig. 16 will be selected. The total efficiency η is composed of the individual efficiencies of the casing η_C, the mechanical losses η_M, losses due to the pipeline η_P, the nozzle η_N, and finally the runner η_R.

$$\eta = \eta_C \cdot \eta_M \cdot \eta_P \cdot \eta_N \cdot \eta_R \tag{17}$$

4.1. Mechanical Loss Estimation

The first consideration includes the mechanical losses in the system, which is a result of frictional losses within the bearings.

The mechanical friction torque M_M can be estimated from the mechanical loading on the bearings due to the force of the jets and weight of the runner. The measured torque M_T use to calculate the efficiency η is given by eq. (18).

$$M_{T(Nj)} = N_j . M_j - M_{M(Nj)} \quad (18)$$

For a number of jets, N_j, where M_J is the torque induced by each jet and M_M is the mechanical friction torque. M_M (19) can be defined as the sum of the bearing friction torque, M_B, which is dependent on which jet is used and the disc friction torque, M_D.

$$M_{M(Nj)} = M_D + M_{B(Nj)} \quad (19)$$

This disc friction torque is defined as the frictional torque arising from the frictional losses of the outer surface of the runner not in contact with the flow passage [4]. The assumption is made that this does not vary with the number of jets used.

4.1.1. Disc friction torque

The disc friction torque can be measured by rotating the turbine shaft at various speeds with and without the runner, since the Pelton used in the test rig at NTUA is the segmented Pelton [18] where the buckets can be removed from the hub, it can be tested with the hub only, and without the hub. During the experimental testing, three additional tests were carried out to measure the torque against the rotational speed at Q = 0 m^3/s with 1) the full runner, 2) only the hub but no buckets and 3) no hub or buckets. Therefore, the torque measured with the runner will be the disc friction torque and without the runner the bearing losses, which can be subtracted from the total. The results of these tests are given in Fig. 17.

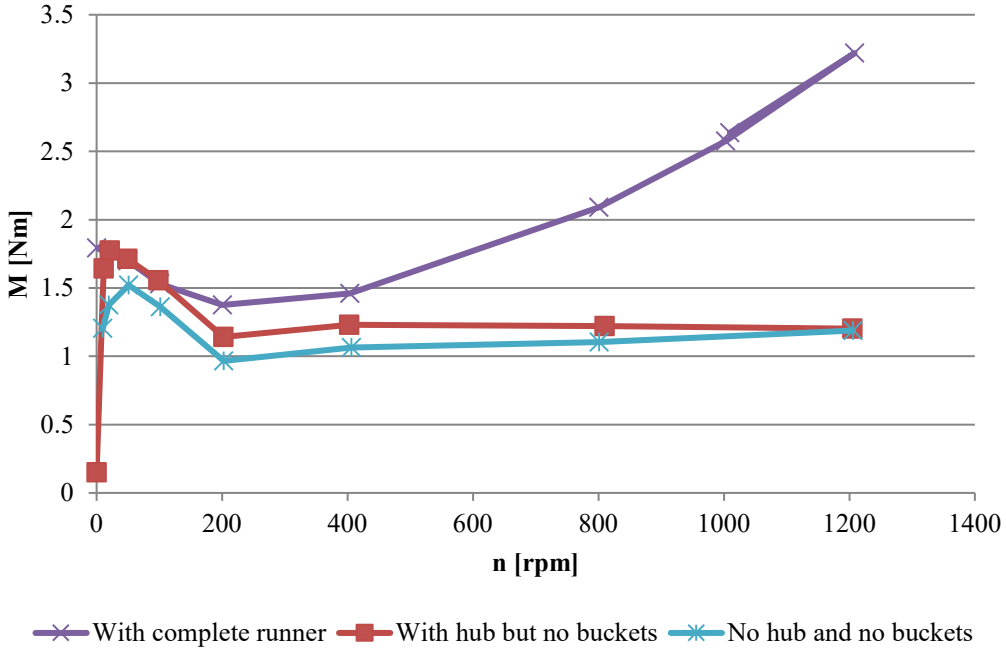

Figure 17. Frictional torque vs rotational speed when Q = 0 m^3/s

Assuming that the bearing friction is not significantly affected by the loading as a result of mass of the runner (23.6 kg), the disk friction, M_D, can be approximated as:

$$M_D = M_f - M_s \quad (20)$$

Where M_f is the friction torque of the full runner in rotation and M_s is the friction torque from only the shaft rotating. At the BEP rotational speed, this gives a disk friction of M_D = 2.4 - 1.1 = 1.3 Nm.

4.1.2. Bearing friction torque, M_B

The hydraulic loads applied to the runner for a twin jet horizontal arrangement are shown in Fig. 18 below, where the loading force $\mathbf{F_J}$, for an ideal jet can be represented as:

$$\mathbf{F_J} = \dot{m} . \mathbf{V} \quad (21)$$

Where $\dot{m}$ is the mass flow rate of the fluid and $\mathbf{V}$ is the velocity vector.

For twin jet machines with an angle θ between the jets, the resultant force of the upper jet, $\mathbf{R_{u1}}$, operation only is given in eq. (22).

$$\mathbf{R_{u1}} = \sqrt{\left(\mathbf{F_J}\cos\beta\right)^2 + (\mathbf{F_J}\sin\beta + W_r)^2} \tag{22}$$

Where W_r is the runner weight (acting vertically downwards) and $\mathbf{F_J}$ us the jet force acting downwards at an angle β to the horizontal. For twin jet operation the resultant forces, $\mathbf{R_{u2}}$ is given in eq. (23).

$$\mathbf{R_{u2}} = \sqrt{(\mathbf{F_R}\cos\alpha)^2 + (W_r - \mathbf{F_R}\sin\alpha)^2} \tag{23}$$

Where $\mathbf{F_R} = \mathbf{2}(\mathbf{F_J}\cos\frac{\theta}{2})$ is the twin jet resultant hydraulic force acting upwards at angle α.

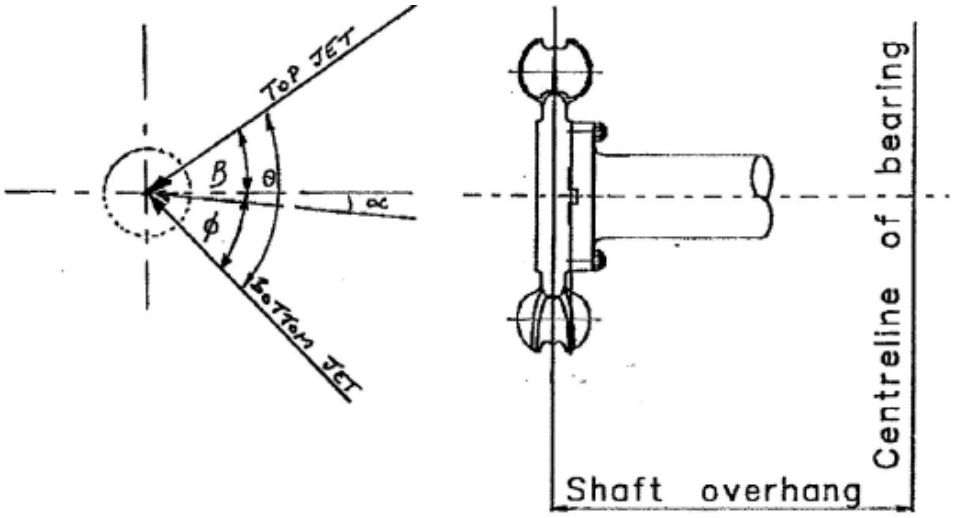

Figure 18. Loads on the runner [19]

Since both the weight and jet loadings are in the same plane, these forces may be considered as radial loads. The axial thrust is very small so will not be calculated in this instance, however thrust bearings are fitted with capability of taking thrust in either direction. Fig. 19 shows the bearing arrangements for the Pelton test rig, taken from the CAD model, and the details for each bearing are given below.

- Bearing 1 – B1 SKF Cylindrical Roller Bearing (SKF N 214 ECP) - designed to support radial loading
- Bearing 2 – B2 SKF Spherical Roller Bearing (SKF 22211 E) - designed to support axial and radial loading

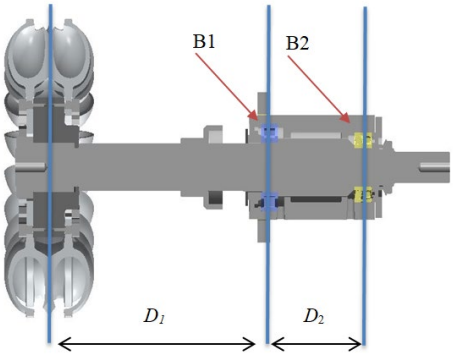

Figure 19. Pelton test rig bearing arrangement

The test rig is equipped with an overhung bearing design with a radial (B1) and thrust (B2) bearing, and the associated bending moment diagram is shown in Fig. 20.

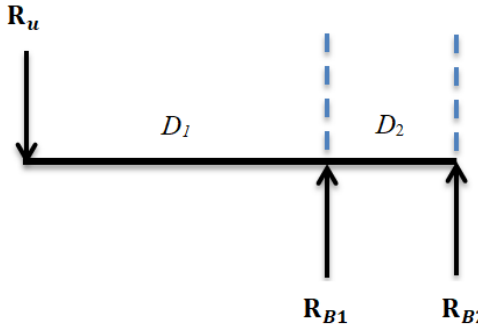

Figure 20. Bending moment diagram for showing radial loads on bearings

Taking moments about B1:

$\mathbf{R_u} \times D_1 = R_{B2} \times D_2$ therefore, $R_{B2} = \frac{\mathbf{R_u} \times D_1}{D_2}$

Taking moments about B2:$\mathbf{R_u} \times (D_1 + D_2) = R_{B1} \times D_2$ therefore, $R_{B1} = \frac{\mathbf{R_u} \times (D_1 + D_2)}{D_2}$

Where, R_{B1} is the load at bearing 1 and R_{B2} is the load at bearing 2.

The forces acting on each bearing at the BEP conditions can be resolved using the equations, as shown in Table 6 below.

Table 6. Bearing forces for single and twin jet operation

		$N_j = 1$	$N_j = 2$
$\dot{m}$	[kg/s]	24.4	48.8
H	[m]	60	60
v	[m/s]	34.3	34.3
$\beta = \phi$	[deg]	40	40
m_r	[kg]	23.6	23.6
W_r	[N]	231.5	231.5
$R_{u1,2}$	[N]	998.2	1298.2
D_1	[mm]	315	315
D_2	[mm]	135	135
R_{B1}	[N]	**3327.3**	**4327.3**
R_{B2}	[N]	**2329.1**	**3029.1**

Once these values have been calculated the online tool *SKF Bearing Calculator* [20] can be used to estimate the bearing friction losses. The tool requires the following input data:

- The radial loads on each bearing- given in Table 6.
- The operating temperature- this was not measured, however a range of values are looked at in order to establish the impact of the temperature on the performance. The value used for the losses was taken as 40°C.
- Viscosity of lubricant- The lubricant used on these bearings is a Lithium soap, LGEP-2, which has a viscosity of 200mm^2/s at 40°C and 16mm^2/s at 100°C.

Thus, the frictional torque as a function of temperature for bearings 1 and 2 is plotted in Fig. 21.

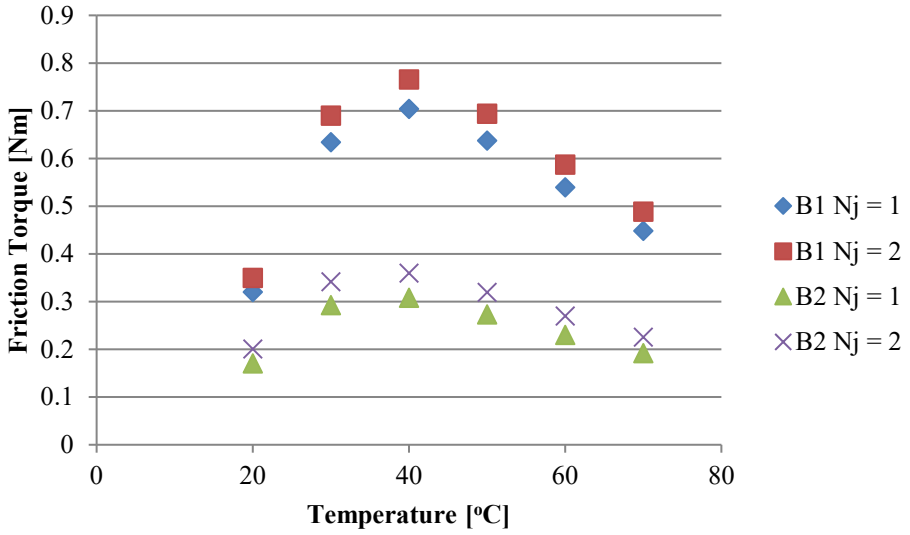

Figure 21. The effect of temperature on bearing friction torque

In order to account for the worst case scenario an operating temperature of 40°C was chosen for the estimation. The resultant bearing friction torques are given in Table 7 below. The losses can be determined using M_B/M_t, where M_t is the total torque measured experimentally.

Table 7. Bearing friction torques and losses approximated from the SKF bearing calculator

		$N_j = 1$	$N_j = 2$
M_{B1}	[Nm]	0.7037	0.7656
M_{B2}	[Nm]	0.3081	0.3595
$M_B = M_{B1} + M_{B2}$	[Nm]	1.012	1.125
M_t	[Nm]	125.09	234.44
M_B/M_t		0.81%	0.48%

4.1.3. Mechanical Friction Torque, M_M

Since the mechanical friction torque, M_M is the sum of the bearing friction from Table 6 and disc friction, calculated in 4.1.1 the value can now be calculated using eq. (19) as follows:

- For single jet operation: $M_{M1} = 1.3 + 1.012 = 2.312$ Nm
- For twin jet operation: $M_{M2} = 1.3 + 1.125 = 2.425$ Nm

Expressing this as a ratio between the friction torque and the total torque, $\frac{M_{M1}}{M_{t1}} = 1.848\%$ and $\frac{M_{M2}}{M_{t2}} = 1.0344\%$, for single and twin jet operation respectively. Therefore the mechanical losses, η_M can be calculated as follows.

$$\eta_M = 1 - \frac{M_{M1}}{M_{t1}} = 98.152\% \tag{24}$$

4.2. Pelton Turbine System Modelling

The full Pelton system can be broken down into three primary regions of analysis, which introduce hydraulic losses that will be experienced as nozzle losses, these are as follows:

1. Pipework Losses - this includes the bifurcation and pipe downstream of the pressure sensor, outlined in 4.2.1
2. Nozzle Losses - this includes the full injector, where the losses at the BEP are predicted using CFD.
3. Runner Losses - this region includes the losses in the runner, which are modelled by combining the real jet velocity profiles as an inlet boundary condition to a runner simulation.

4.2.1. Pipeline Losses, η_P

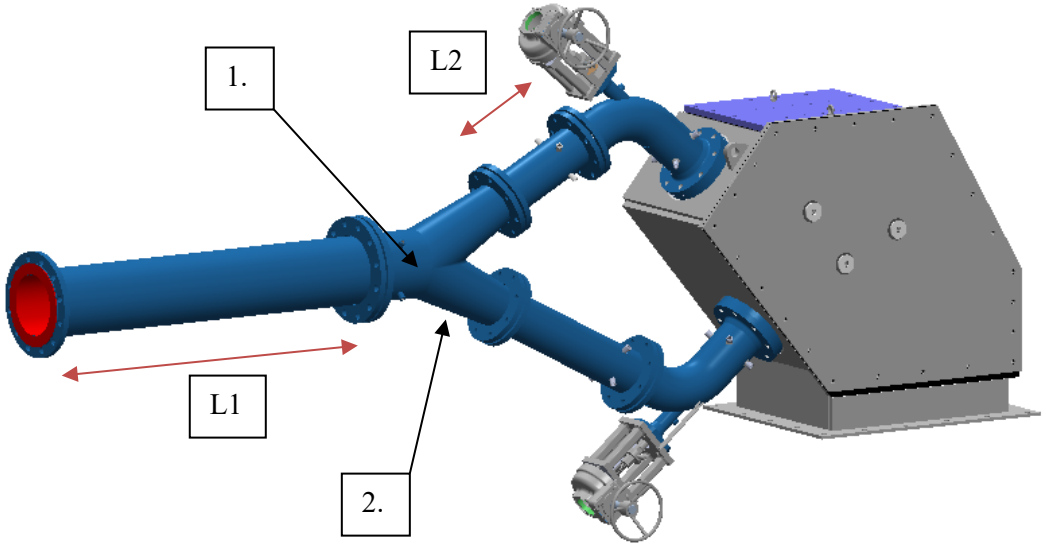

Figure 22. Pelton test rig loss features and straight pipe sections for 1

The flow in 1. can be generally assumed to follow well established phenomenological equations and can be approximated by examining the individual head losses for each component using the loss factors *K*.

$$h_l = K.\frac{v^2}{2g} \tag{25}$$

Where *v* is the mean velocity in the pipe calculated from the internal diameter and the mass flow rate, which for the pipe L1 with 196 mm i.d. is calculated as 0.8 m/s and L2 with 128 mm i.d. is calculated as 1.88 m/s.

Region 1 can be broken down into 2 different loss features and 2 straight pipe sections as shown in Fig. 22. The loss features are defined as:

1. **Bifurcation:** This is treated as a 45deg metre bend as the lower injector is closed.
2. **Gradual contraction:** this is the section where the pipe diameter steps down from bifurcation to the 128 mm diameter pipe.

The loss factors (*K)* are given in for each feature and from these the head loss, h_l, can be calculated using eq. (25). The head loss for each feature as well as the total head loss is shown in Table 8 below.

Table 8. Head loss from loss features

Loss feature	**Loss factor (*K*)**	**Head loss (h_l)**
1	0.20	0.036m
2	0.04	0.0072m
	Total	**0.043m**

The head loss from the straight pipe sections can be calculated using the following.

$$h_l = \frac{4flv^2}{2Dg} \tag{26}$$

Where *l* is the total pipe length, (*l1 +l2*), which is measured as 1.25 m and 0.39 m respectively, *D* is the pipe diameter. *f* is the Fanning friction factor determined by the surface roughness and Reynolds number. The relative surface roughness is equal to the average height of surface irregularities divided by the pipe diameter, a conservative estimate of the average height of irregularities from the corrosion on the inside of the pipe would put this number somewhere in the region of 3 mm, which results in a relative roughness of 0.02. Therefore, *f*, is taken from a Moody diagram as 0.0123. This gives a head loss from the pipe section L1 = 0.0103 m and from L2 = 0.0267 giving a total as 0.037 m. The total head loss through region 1 can then be taken as 0.043 + 0.037 = 0.08 m, which equates to **0.13%** loss from the 60 m inlet pressure.

4.2.2. Nozzle Losses, η_N

The nozzle losses can be determined using a CFD analysis of the full 3D injector at the BEP, outlined in previous published work by the authors. The standard injector design highlighted in Fig. 23, consists of a single injector for each of the three nozzle and spear combinations. The geometry of interest includes the nozzle, spear, spear rod, three spear holding vanes and the 60° pipe bend. The losses are calculated as **1.8%.**

4.2.3. Runner Losses, η_R

One method of quantifying the nozzle and runner losses has already been explored by the authors in [21]. In this paper the real water jet profiles obtained from the 3D injector simulation, shown in Fig. 23 at the BEP head and flow rate were imported into the runner simulation, shown in Fig. 24, therefore calculating the losses from the point beyond the bifurcation to the runner. This method therefore neglects the upstream losses beyond the bifurcation and the mechanical losses, however since these have already been approximated and measured respectively, they can be added to the nozzle and runner losses and by doing so the casing losses may be ascertained.

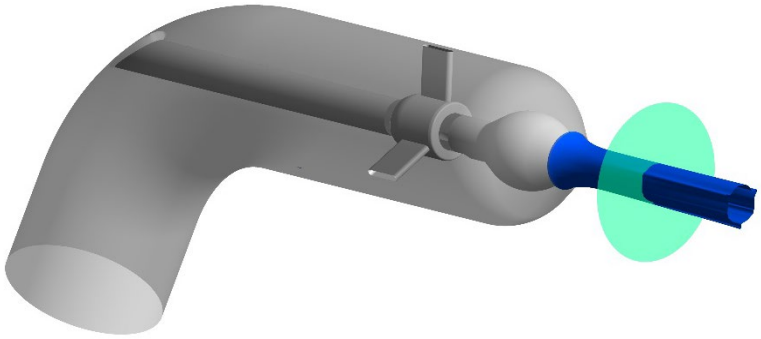

Figure 23. 3D injector simulation showing the plane used in the analysis.

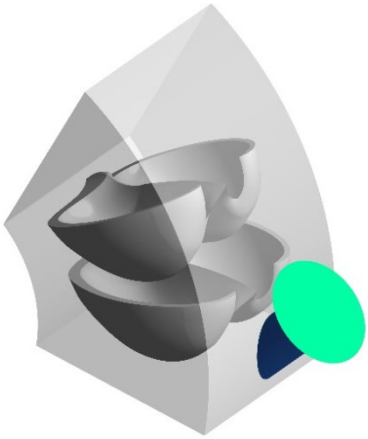

Figure 24. 3D runner simulation showing the corresponding plane used in the analysis.

The efficiency obtained for has now been normalised to **100%** for comparative purposes.

4.3. Total Efficiency Analysis

The total numerical hydraulic efficiency, η_{nh}, accounting for all the losses in the Pelton system can be calculated using eq. (27) where η_R is normalised to 100%.

$$\eta_{nh} = \eta_P.\eta_N.\eta_R = 99.87 \times 98.2 \times 100 = 98.1\ \% \qquad (27)$$

The experimental hydraulic efficiency, η_{eh}, excluding the mechanical losses, η_M calculated in eq. (24), can be calculated from the measured experimental efficiency, η, which has been normalised against η_R, as follows.

$$\eta_{eh} = \frac{\eta}{\eta_M} = \frac{98.58}{98.152} = \mathbf{100.44\%} \qquad (28)$$

What this result shows is that the numerically predicted efficiency was 0.44 % lower than the efficiency, which was experimentally measured and corrected for the losses. This discrepancy is within the total uncertainty of the experiment as estimated in section 2.1. Since the splashing and water interference effect caused by the casing was not included in the CFD model it was expected that numerical results would over predict the efficiency. This indicates that either the CFD model is under predicting the torque or the mechanical or injector losses have been overestimated or more likely a combination of all of these factors.

Since the numerical and experimental results lie very close to each other and are both within the same margin of error another conclusion that can be made is that the effect of the casing is practically negligible for this casing width. This would explain the flattening of the curves of efficiency with casing width, shown in Fig. 16 as the casing tends towards the widest width. Secondly, these simulations were carried out using a 2-bucket model, which was found during the periodicity study in to give slightly lower efficiencies (0.12%) compared with the equivalent 6-bucket case. This suggests that using more buckets will increase the numerical efficiency. It is recommended that a larger runner section be

modelled with a finer mesh in order to achieve a more accurate absolute numerical result although this will introduce a much higher computational cost.

5. Conclusions

This paper has presented how the FLUENT CFD code can be used to simulate flow within the casing of Pelton turbines. Despite good visual correlation it is not yet possible to obtain a quantitative measure of efficiency using the presented method, therefore experimental model testing is required to ascertain improvements from the suggested design changes. One of the key disadvantages of this method is the long simulation timescales, which makes it unfeasible to compare results from a range of designs. Moreover, to obtain high fidelity models a denser mesh, smaller timestep and higher order discretisation methods, than those initially chosen would be required. Accordingly, compromises have to be made, which introduce numerical errors that falsely modify the flow features.

This paper has attempted to ascertain the absolute efficiency losses due to the casing by examining the differences in the numerical and experimental efficiencies. This was done by estimating the mechanical losses of the Pelton test rig in order to calculate the experimental hydraulic efficiency, η_{eh}. The losses in the pipework upstream of the injector were then estimated using pipe flow equations which were combined with the losses through the full 3D injector and the runner simulation using the real jet profile giving the numerical hydraulic efficiency, η_{nh}. Comparing these two values showed the numerical models to be under predicting the efficiency by 0.44%, which is inside of the total experimental uncertainty of 0.6% and the total numerical uncertainty of 0.97%.

From this several conclusions can be drawn, firstly it is likely that the numerical torque is being under predicted and several reasons for this have been outlined. Another possibility is that at the standard design casing width the effects are largely negligible, however it was established that there are potential difference of ≈3% in efficiency from the widest to narrowest casing widths.

Nevertheless, the CFD model has been shown to be a good predictor of casing flow, such that a number of baffles and shrouds were proposed, which had a positive impact on performance. Furthermore, casing width has been investigated and it was found that there appears to be a linear relationship with efficiency and that casing dimensions have a greater overall impact on efficiency than the addition of baffles and shrouds.

It is envisaged that with time CFD modelling of Pelton turbines will continue to improve, however as yet it still can only be used as a design tool to make predictive improvements to casing design.

Acknowledgements

The authors would like to thank Gilbert Gilkes & Gordon Ltd, Lancaster University Renewable Energy and Fluid Machinery Group and the Laboratory of Hydraulic Turbomachines, NTUA.

References

[1] T. Staubli, P. Weibel, C. Bissel, A. Karakolcu and U. Bleiker, "Efficiency increase by jet quality improvement and reduction of splashing water in the casing of Pelton turbine," in *16th International Seminar on Hydropower Plants*, Vienna, 2010.

[2] M. Neuhauser, F. Leboeuf, J. C. Marongiu, E. Parkinson and D. Robb, "Simulations of Rotor-Stator Interactions with SPH-ALE," in *Advances in Hydroinformatics: SIMHYDRO 2012 - New Frontiers of Simulation*, Springer Hydrogeology, 2012, pp. 349-361.

[3] M. Rentschler, M. Neuhauser, J. C. Marongiu and E. Parkinson, "Understanding casing flow in Pelton turbines by numerical simulation," *IOP Conf. Series: Earth and Environmental Science,* vol. 49, 2016.

[4] International Electrotechnical Commission, "Hydraulic turbines, storage pumps and pump-turbines - Model acceptance tests," IEC, 1999.

[5] A. Perrig, "Hydrodynamics of the Free Surface Flow in Pelton Turbine Buckets," Ecole Polytechnique Federale de Lausanne, Lausanne, 2007.

[6] A. Santolin, G. Cavazzini, G. Ardizzon and G. Pavesi, "Numerical investigation of the interaction between jet and bucket in a Pelton turbine," *Proceeding IMechE Journal A: Power and Energy,* vol. 223, 2009.

[7] V. Gupta, V. Prasad and R. Khare, "Numerical simulation of six jet Pelton turbine model," *Energy,* vol. 104, pp. 24-32, 2016.

[8] A. Zidonis and G. A. Aggidis, "State of the art in numerical modelling of Pelton turbines," *Renewable and Sustainable Energy Reviews,* vol. 45, pp. 135-144, 2015.

[9] B. E. Launder and D. B. Spalding, "The Numerical Computation of Turbulent Flows," *Computer Methods in Applied Mechanics and Engineering,* vol. 3, pp. 269-289, 1974.

[10] P. J. Roache, "Perspective: A Method for Uniform Reporting of Grid Refinement Studies," *ASME J. Fluids Eng.,* vol. 116, pp. 405-413, 1994.

[11] F. R. Menter, "Two-equation eddy-viscosity turbulence models for engineering applications," *AIAA,* vol. 32, no. 8,

pp. 1598-1605, 1994.

[12] J. U. Brackbill, D. B. Kothe and C. Zemach, “A Continuum Method for Modeling Surface Tension,” *Journal of Computational Physics,* vol. 100, no. 2, pp. 335-354, 1992.

[13] Z. Zhang, LDA Application Methods - Laser Doppler Anemometry for Fluid Dynamics, Springer, 2010.

[14] M. Raffel, C. E. Willert, S. Wereley and J. Kompenhans, Particle Image Velocimetry A Practical Guide, Springer, 2007.

[15] M. Nechleba, Hydraulic Turbines: Their Design and Equipment, Prague: Artia, 1957.

[16] L. Quartz and K. Meerwarth, Wasserkraftmaschinen: Eine Einführung in Wesen, Bau und Berechnung von Wasserkraftmaschinen und Wasserkraftanlagen, Berlin und Heidelberg: Springer-Verlag, 1963.

[17] J. Raabe, Hydraulische Maschinen und Anlagen. Teil 2 Wasserturbinen, Düsseldorf: VDI-Verlag, 1970.

[18] G. A. Aggidis and R. Cattley, “Fastening of Pelton turbine buckets”. European Patent 1452731, September 2004.

[19] Gilbert Gilkes and Gordon Ltd, “Technical Design Manual Section 820 Horizontal Shaft Pelton Turbines,” 2015.

[20] SKF Group, “SKF Bearing Calculator,” [Online]. Available: http://webtools3.skf.com/BearingCalc/. [Accessed 15 05 2018].

[21] S. Petley, A. Zidonis, A. Panagiotopoulos, D. Benzon, G. A. Aggidis, J. S. Anagnostopoulos and D. E. Papantonis, “Out With the Old, in With the New: Pelton Hydro Turbine Performance Influence Utilizing Three Different Injector Geometries,” *ASME J. Fluids Eng.,* vol. 148, no. 8, p. 081103, 2019.